Chemical
Science

EDGE ARTICLE

View Article Online
View Journal | View Issue

Check for updates

Cite this: *Chem. Sci.*, 2026, **17**, 3043

All publication charges for this article have been paid for by the Royal Society of Chemistry

Revealing the kinetic limits of sodiation and lithiation at hard carbon using the diluted electrode method

Yuki Fujii, Zachary T. Gossage, Ryoichi Tatara and Shinichi Komaba*

Electrochemical sodium and lithium insertion into hard carbon (HC) relies on two main reactions: adsorption/intercalation and pore-filling. The rates of these two reactions are key to attaining high power densities and fast charging in batteries, but distinguishing the rate limitations can be challenging due to their overlap and issues with Na^+ and Li^+ transport in conventional composite electrodes. Herein, we focus on the usage of the diluted electrode method to better evaluate the kinetics of electrochemical sodiation and lithiation in HC. Through galvanostatic charge/discharge testing, cyclic voltammetry and potential step analysis performed on diluted HC-electrodes in aprotic Na- and Li-cells, we confirm that the sodium-insertion rate into HC is faster than the lithium-insertion rate when we consider both adsorption/intercalation and pore-filling reactions. The apparent ion diffusion coefficients, D_{app}, are on the order of 10^{-10}–10^{-11} and 10^{-10}–10^{-12} $cm^2\ s^{-1}$ for sodium and lithium insertion, respectively. Furthermore, sodiation into the diluted HC-electrode showed comparable rate capability and D_{app} to lithium intercalation at diluted graphite electrodes. In addition, we evaluated the temperature dependence using potential-step and electrochemical impedance methods, finding that activation energies, E_a, were ~55 and ~65 kJ mol^{-1} for sodiation and lithiation, respectively. We find reactions in the solid state, *i.e.*, nucleation of pseudo-metallic clusters, as well as the charge transfer at the electrolyte/HC interface can limit the rate performance in diluted HC electrodes.

Received 7th October 2025
Accepted 23rd November 2025

DOI: 10.1039/d5sc07762a

rsc.li/chemical-science

Introduction

Currently, hard carbon (HC) is the most promising candidate for the negative electrode of sodium-ion batteries (SIBs).[1] The structure of HC consists of thousands of turbostratic basic structural units combined together to create a network of pseudo-graphitic layers and pores.[2,3] These structures have been essential to attaining high reversible capacities for HCs in SIBs in recent years, leading to comparable energy densities to lithium-ion batteries (LIBs) using $LiFePO_4$//graphite.[4,5] The sodiation mechanism has been reported as two main steps, including: (1) insertion into the interlayer space of the pseudo-graphitic domains and adsorption onto defect sites above 0.1 V and (2) pore filling with Na–Na bonding that produces pseudo-metallic clusters below 0.1 V.[3,6] Likewise, LIBs can also utilize this pore-filling mechanism with HC to attain reversible capacities even beyond graphite (over 500 mAh g^{-1}).[2,7,8] Furthermore, HC is well known to provide high-rate capabilities and considered to be fast compared with intercalation chemistry at graphite.[9] However, utilizing the pore-filling mechanism at high rates can be difficult due to closeness of the reaction potential to alkali metal plating,[10] and generally no plateau is observed for the lithium insertion process. We have found that this plateau potential can be controlled to an extent *via* the synthesis methods.[2,11] While the precise HC structure may impact the rate performance for different alkali ions,[2] there is interest to compare the rate capabilities for single active materials to better understand the relationship between the structure and rate performance.

Often, high-rate galvanostatic testing is performed using coin cells or 3-electrode cells to evaluate the power capability of electrode materials. However, this can underestimate the active material rate capabilities due to concentration overvoltage within the composite electrode during the high rate operation,[12,13] where guest-ion depletion or saturation of the electrolyte occurs within the porous electrode. To more effectively evaluate the kinetics of the insertion materials, model electrodes such as single particles, thin films or monolith materials can be utilized.[14–17] Besides, Ariyoshi *et al.* proposed the usage of a diluted electrode method where some of the active material within the composite electrode is exchanged for an electrochemically inactive material, *i.e.* Al_2O_3.[18–22] Under these conditions, the separated particles of active materials can utilize sufficient amounts of nearby ions to reach a high state-of-charge (SOC) or depth-of-discharge (DOD) under high-rate insertion conditions.[18,19] This diluted electrode method can evaluate any type of particle while maintaining the composite

---

Department of Applied Chemistry, Tokyo University of Science, Shinjuku, Tokyo 162-8601, Japan. E-mail: komaba@rs.tus.ac.jp

electrode structure, including the porosity and binder effects. Recently, our group has been using this method to evaluate HC for SIBs, where fast sodiation rates of ∼4C show reversible capacities of *c.a.* 200 mAh g^{-1}, or ∼85% of the capacity at 0.1C insertion rates.[1,23] This makes the diluted electrode method suitable for a detailed comparison of HC for SIBs and LIBs to better understand the relationship between the rate and the energy storage mechanism. There are major interests to understand this relationship,[24] but there have been no studies comparing sodiation and lithiation rates at HC using the diluted electrode method.

In this study, we conduct a variety of electrochemical analyses using the diluted electrode method to compare the sodium- and lithium-insertion kinetics of a commercial HC electrode. We find unique behavior at low and high galvanostatic charging (reduction) rates, attributed to the redox of HC, and show that our method avoids issues of concentration overvoltage in the composite electrode. At low rates, both the adsorption/insertion and pore-filling mechanism are observed, while only adsorption and insertion occur at high charging rates. In addition to galvanostatic testing, the diluted HC-electrodes were examined using cyclic voltammetry, potential step chronoamperometry, and electrochemical impedance spectroscopy. Based on these various analyses, the sodiation rates were determined to be faster than lithiation of this HC, especially for the pore filling mechanism and during operation below room temperature. On the other hand, at very high rates with non-diluted electrodes, lithium tended to maintain a higher capacity, which may be related to the larger adsorption and insertion capacities for lithium. Overall, the rate of insertion will be majorly limited by the charge-transfer resistance and solid-state diffusion in HC particles. Therefore, a key point of focus for developing improved HC materials for SIBs and LIBs is to attain faster kinetics of the pore-filling process so that they can be accessed at high charging rates.

Experimental section

Electrode preparation

For preparing the composite electrodes, HC powder (Carbotron® P (J), Kureha Battery Materials Japan) was used as the active material. Material characterization experiments of this HC are shown in the SI (Fig. S1 and S2). α-Aluminum oxide powder (Al_2O_3, Wako Pure Chemical Industries Ltd) acted as the dilutant, and sodium polyacrylate (Kishida Chemical Co., Ltd) was used as the binder. Table S1 shows mass compositions of diluted HC-electrodes. These powders were mixed at various ratios based on volume, with HC : dilutant : binder of $x : 95 - x : 5$ vol/vol. The volume ratio of HC contained in the electrode, x, is defined as the HC concentration [vol%]. The volume of the components was calculated based on true densities of each materials, where Carbotron P (J), Al_2O_3, and sodium polyacrylate were 1.52, 3.97, and 1.3 g cm^{-3}, respectively.[25–27] Additionally, single-walled carbon nanotubes (SWCNTs, Lamfil®, Kusumoto Chemicals) were used as the conductive additive. The as-received product consisted of deionized water : SWCNTs : sodium carboxymethyl cellulose (CMC) in a weight ratio of 99 : 0.4 : 0.6. Therefore, 100 μL of this dispersion has a total SWCNT mass of ∼0.4 mg. The aqueous slurry containing HC, Al_2O_3, binder, and SWCNT was cast on aluminum foil (20 μm, Hohsen) or copper foil (18 μm, Hohsen) and dried under ambient conditions. The dried composite electrodes were cut into 10 mm disks and pressed with a mono-axis pressure of ∼250 MPa (Specac) to obtain a thickness of 40–47 μm (after subtracting the current collector thickness). The prepared electrodes were dried at 150 °C overnight before cell assembly. The homogeneity of the mixed composite electrode was evaluated using scanning electron microscopy (JSM-IT800SHL, JEOL). The electric conductivity of unpressed/pressed composite electrodes was evaluated by using a resistivity meter Loresta-GX (MCP-T700, Mitsubishi Chemical Analytech, Co. Ltd) with a PSP probe (RMH112, 1.5 mm pins-distance).

Electrochemical cells

R2032-type coin-cells (Hosen) were assembled using the prepared composite electrode as the working electrode in an Ar-filled glove box. Freshly cut metallic Na (99.9%, Kanto Chemical) was directly immersed in the electrolyte solution, rolled into a thin sheet, and punched into 14 mm (diameter) disks to use as the counter electrode. 1 mol dm^{-3} $NaPF_6$ in ethylene carbonate and diethyl carbonate (1 : 1 v/v) (battery grade, Kishida Chemical) and a glass fiber filter (GB-100R, ADVANTEC) were used as the electrolyte and separator, respectively. Likewise, Li-cells were prepared in a similar manner using Li metal (99.8%, Honjo Chemical) and 1 mol dm^{-3} $LiPF_6$ in ethylene carbonate and dimethyl carbonate (1 : 1 v/v) (battery grade, Kishida Chemical) as the counter electrode and electrolyte solution, respectively.

Electrochemical measurements

Galvanostatic charge–discharge was carried out on the coin-cells using a battery cycler (TOSCAT-3100, TOYO system). The initial three cycles were conducted applying 25 mA g^{-1} for charge/discharge at 25 °C. The lower cut-off voltage was fixed at 2 mV (*vs.* Na or Li), and the upper cut-off voltage was set to 1.25 V and 1.0 V for Na and Li cells, respectively. Between each charge and discharge step, the cell was allowed to rest at the open circuit for a period of 5 minutes. After the initial three cycles, the current was systematically increased up to 25 000 mA (g of active material)$^{-1}$. Lower currents of 5 and 10 mA g^{-1} were employed for tests at 10 °C. For comparative analysis, the reversible capacities were normalized based on the reversible capacity obtained at 25 mA g^{-1}. Using the rate-test data, the apparent diffusion coefficients (D_{app}) were estimated from the slopes in the capacity–current curves based on a spherical diffusion model using OriginPro® (version 2025, OriginLab).

Cyclic voltammetry (CV), potential-step chronoamperometry (PSCA), and electrochemical impedance spectroscopy (EIS) were performed on Na or Li coin-cells (half-cells) with a multi-potentiostat (VMP3, BioLogic). During CV, the HC potential was swept between 1.0 V and 2 mV at a scan rate of 20 μV s^{-1} at 25 °C. The scan rate was subsequently increased up to 5 mV s^{-1} to evaluate the scan-rate dependence. PSCA was performed on a 5 vol% HC-electrode using cathodic potential steps from 1.0 V to 0.1 V and from 0.1 V to 2 mV, re-oxidized using potential steps from 2 mV to 0.12 V and then stepped to 1.0 V. D_{app} values were extracted from slopes of the linear part in $\ln(i) - t$ curves of the chronoamperogram data again based on a spherical diffusion model (calculated using OriginPro® version 2025, OriginLab). EIS was also performed on Na and Li half-cells by applying ±10 mV amplitude AC voltage at different bias voltages (OCV; 0.5, 0.06, and 0.015 V). For the EIS measurements, the cell was reduced galvanostatically using a current of 25 mA g^{-1} followed by a potential hold for 1 hour. Additionally, a 3-electrode cell (TOYO system) and a potentiostat (Squidstat Plus, Admiral Instruments) were used for EIS data collection. The fittings of Nyquist plots were performed using Z-Fit in EC-Lab version 11.61 (BioLogic). The temperature dependencies of Na/Li insertion were evaluated by PSCA and EIS after the high current testing in a range from 10 to 40 °C.

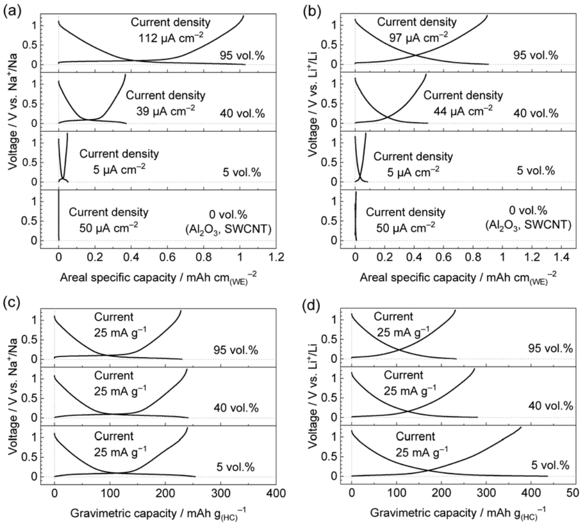

Fig. 2 Galvanostatic charge–discharge curves of HC diluted electrodes in Na and Li cells. (a and b) Areal specific capacities and (c and d) gravimetric capacities are plotted based on the HC mass.

Results and discussion

Electrochemical characterization

Prior to conducting kinetic analysis of HC for LIBs and SIBs, we prepared and characterized diluted electrodes with varied amounts of diluent and active materials in the composite electrodes. Herein, the diluted electrodes are referred based on the active material content, *i.e.* 5 vol% indicates a composite electrode containing 5 vol% active material, 5 vol% binder and conductive additive, and 90 vol% Al_2O_3 both in Na and Li cells. The SEM observation in Fig. 1 and S3 confirms the homogeneous dispersion of HC and Al_2O_3 particles. Notably, in the 5 vol% HC-electrode, there was no HC aggregation with the HC particles isolated by the surrounding Al_2O_3. We note that the electronic conductivity was decreased by dilution with Al_2O_3, but conductivities >100 S m^{-1} were maintained even in the pressed 5 vol% HC-electrode with 90 vol% Al_2O_3. These values are comparable to reported electric conductivity of electrodes for lithium-ion batteries,[28,29] and we ensured a good electronic pathway within the diluted electrodes by using SWCNTs. The diluted HC-electrodes were characterized using galvanostatic charge–discharge and CV analyses. As shown in the charge/discharge curves in Fig. 2a and b, dilution with Al_2O_3 leads to an equivalent loss in the areal (and volumetric) capacities. In all cases, the electrochemical profile is maintained with voltage-slope and voltage-plateau regions, which are typically observed for HCs. Besides, the pure diluted electrodes (95 vol% Al_2O_3 and 0 vol% active material) show virtually no reversible capacities in both Na and Li cells. In Fig. 2c and d, the data are replotted using gravimetric capacities of the active materials (details are shown in Table S2). Slow constant-current charging with 25 mA $g_{(HC)}^{-1}$ shows constant values, ~240 mAh $g_{(HC)}^{-1}$ and ~300 mAh $g_{(HC)}^{-1}$ in Na and Li cells, respectively, for both diluted and conventional electrodes, which is consistent with previous reports.[7,23,30,31] For Na (Fig. 2c), the reversible capacities were similar regardless of the HC concentration, indicating good electronic conductivity, ionic conductivity and porosity inside of diluted composite electrodes. Furthermore, there was negligible voltage hysteresis between charge and discharge, indicating negligible ohmic drop and high reversibility of the reaction.[3] For Li (Fig. 2d), the gravimetric capacities increased under dilution, which seem to be related to the pore-filling capacity.[7] In addition, because SWCNT conductive additives can show double layer capacitance, the obtained capacities can be corrected by subtraction of the

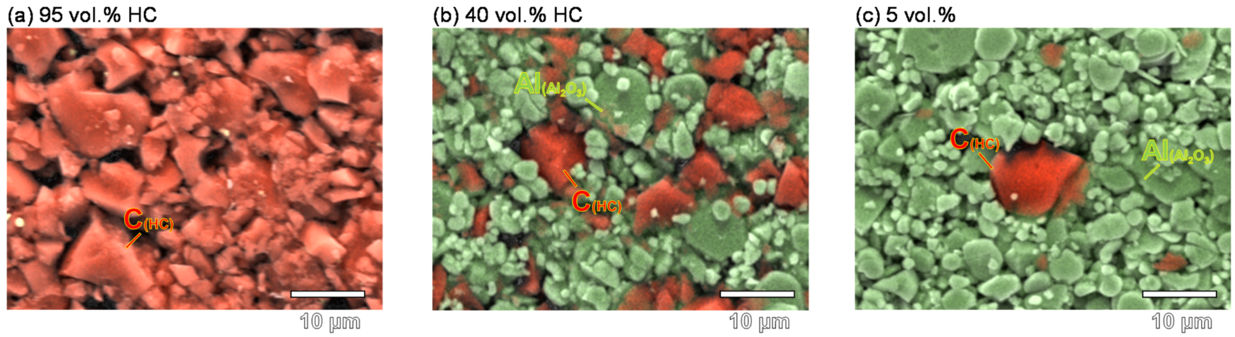

Fig. 1 SEM images obtained from the top view of composite electrodes containing (a) 95 vol%, (b) 40 vol%, and (c) 5 vol% HC. All images were taken by energy dispersive X-ray spectroscopy (EDX) mapping at ×2500 magnification. C in HC and Al in Al_2O_3 are highlighted in red and green, respectively.

SWCNT capacity from the total capacity of the diluted electrode, as shown in Fig. S5 and Table S2.

Galvanostatic charge–discharge of cells at tiny currents have been reported to suffer from parasitic capacity losses at tiny currents.[22,32] To determine the lower limit of HC concentration that allows us to evaluate (de)insertion without significant side reaction, Na and Li coin cells were further investigated using CV (Fig. 3). A slow scan rate of 20 μV s^{-1} was used to determine the redox peaks and precisely compare the current of the HC-electrodes. In the Na cell, the redox peak splitting was continuously suppressed through electrode dilution from 95 to 5 vol% HC, attaining a stable peak current of ∼150 mA g^{-1} for the cathodic- and anodic-peaks at 0.05 V and 0.1 V, respectively. As no further improvements were observed lower than 5 vol%, this strongly suggests that the sodium ion depletion in the interstitial space of the composite electrode is resolved. Therefore, the measured insertion/extraction rates become limited by charge-transfer resistance and solid-state diffusion of sodium in the HC particles.[1,18,23]

In contrast, Li cells showed only minor improvements in their electrochemical behavior under dilution conditions. The cathodic currents prior to plating ranged from 100 to 200 mA g^{-1} similar to the Na cells, but no cathodic peak was observed even in the diluted electrode. We believe this is due to the pore filling mechanism occurring at lower potentials close to E° (Li^+/Li).[7] Still, a small negative shift of the anodic peak potential and some increase in the peak current were observed by electrode dilution. We note this minimal improvement in the Li cell implies that the lithium insertion/extraction rates of HC are not limited by the concentration overvoltage caused by depletion of Li^+ within the composite electrode. Rather, the rates seem to be more dominated by ion transfer at the particle surface or within the HC particles, *e.g.* solid-state lithium diffusion. In the 2 vol% HC-electrode in Li cells, HC redox peaks were deformed by the side-reaction capacity on SWCNTs. Therefore, we can conclude that 5 vol% HC-electrodes are suitable to compare the sodiation and lithiation kinetics of HC.

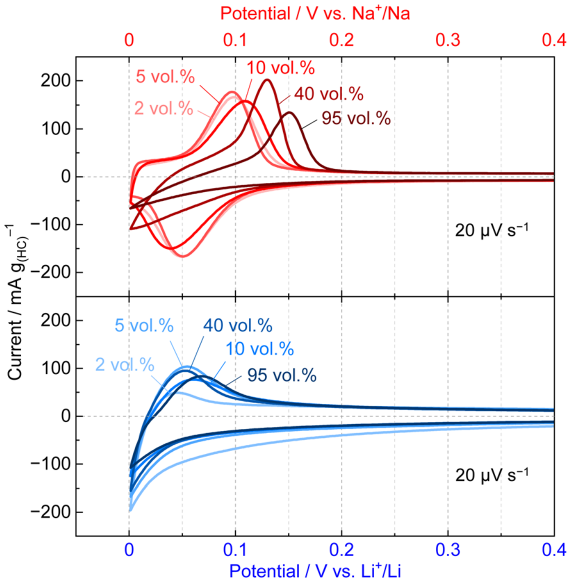

Fig. 3 Cyclic voltammograms of (top) Na and (bottom) Li cells using various diluted electrodes with a scan rate of 20 μV s^{-1}.

Rate-capability testing

Next, we evaluated the rate-performance of our diluted electrodes (5 vol%) and conventional electrodes (95 vol%) in Na and Li cells. As discussed in the introduction, conventional electrodes can show issues with ion supply to the active material at high charging (reduction) rates, while diluted electrodes can alleviate this transport issue to endure higher rates, as illustrated in Fig. 4a. Such measured rates should be closer to the innate rate of the active material. As shown in the reduction curves for sodiation in Fig. 4b, low-currents of ≤25 mA $g_{(HC)}^{-1}$ showed constant values, ∼240 mAh $g_{(HC)}^{-1}$ in Na cells for both diluted and conventional electrodes. Thereafter, the reduction current was sequentially increased to 1000 mA g^{-1}, while the oxidation process was carried out using a constant slow rate of 25 mA g^{-1}. As the reduction current increased, the plateau capacity decreased along with polarization attributed to the ohmic drop and electrochemical impedance, *e.g.* the charge-transfer resistance and ion diffusion in the electrolyte, inside HC and at their interface. Likewise, in the Li cell, diluted electrodes showed reduced polarization and could obtain higher capacities at higher rates compared with conventional electrodes.

The compiled results for the Na and Li cells are shown in Fig. 4d and e, respectively, normalized to the capacities obtained at a slow rate of 25 mA g^{-1}. For Na cells, the undiluted electrode shows a rapid loss in accessible capacity to ∼40% at relatively slow rates of ∼100 mA $g_{(HC)}^{-1}$ (or ∼0.4C) due to increased polarization and loss of access to the full voltage plateau. At even higher rates, the accessible capacity continued to gradually decrease toward <10% at 2236 mA $g_{(HC)}^{-1}$. On the other hand, 10 vol% and 5 vol% HC-electrodes demonstrated improved rate performance that did not show such polarization limitations. They could obtain 80% and 40% of the HC capacity at rates of 1000 and 2500 mA $g_{(HC)}^{-1}$, respectively. Overall, the rate-capabilities of the diluted electrodes were much higher than those of undiluted electrodes, suggesting the rate is becoming limited by sodium insertion into HC.[19,23]

The rate performance of lithium insertion was evaluated in the same manner (Fig. 4e) and normalized with ∼300 mAh $g_{(HC)}^{-1}$ obtained from cycling at 25 mA g^{-1}. The improvements by dilution were much less noteworthy compared to the Na cell, and the capacities faded to ∼60% before 200 mA g^{-1} even in diluted HC-electrodes. The more negative potential of the lower voltage-plateau attributed to their thermodynamics is one of the factors resulting in less improvement in dilution. However, after this initial loss in capacity, the remaining capacities (>40%) could be sustained up to 1000 mA g^{-1} regardless of the HC concentration (Fig. 4e). Although the diluted electrodes tended to perform better with sodium, concentrated electrodes with >40 vol% HC showed comparable rate-performances to the diluted electrode in the Li cell, especially >500 mA g^{-1}. This is a bit unexpected, considering that Na^+ transportation in the electrolyte is faster than Li^+ due to its smaller Stokes radius and

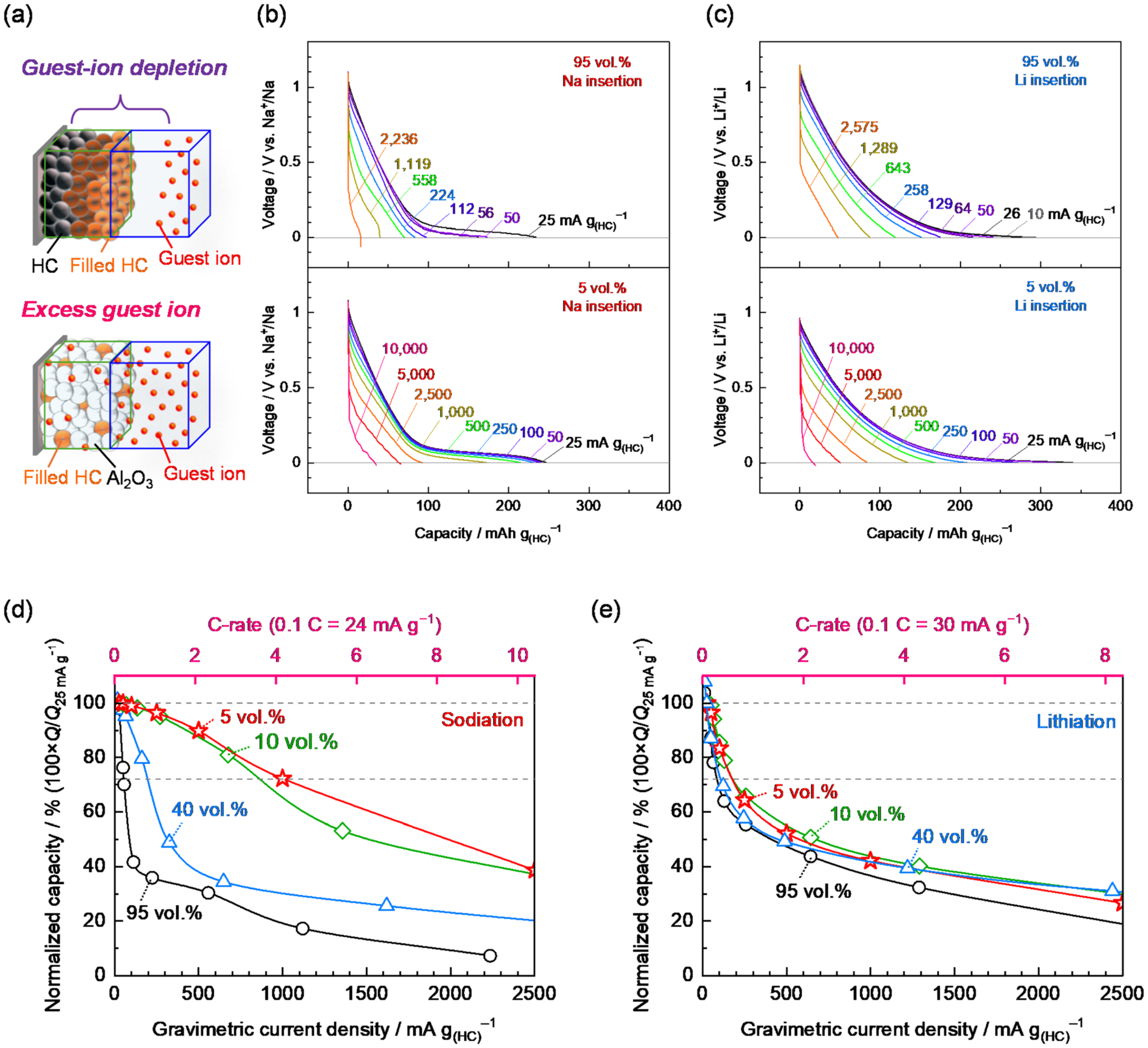

Fig. 4 Rate testing at room temperature using electrodes at various HC concentrations. (a) Schematic image of the electrode condition during high-rate reduction. Charge–discharge curves of undiluted and diluted HC-electrodes in (b) Na cells and (c) Li cells. Rate capabilities of HC electrodes during the insertion process for (d) sodiation and (e) lithiation.

less concentration overvoltage for the Na cell.[33,34] There can also be other factors that impact the final rate performance such as the complex resistance at a high HC concentration as discussed later (Section 3.4). Furthermore, the relatively smaller activation energy correlates with the SEI on the conventional electrode,[35] and the capacity of the sloping region (above 0.1 V *vs.* Li^+/Li) for lithiation is relatively large compared with sodiation, and this seems to enable such higher rate capability. We speculate that this not only may be related to the SEI, which are known to be different for Na and Li systems,[36] but also may be influenced by the diluted electrode structure where a homogeneous SEI can be formed on HC particles similar to microelectrodes.[37]

For additional quantification of the insertion kinetics of sodium and lithium into the 5 vol% HC-electrodes, the apparent diffusion coefficients (D_{app}) were estimated from the rate–capability curves using eqn (1).[20,38,39]

$$Q = \frac{Ca}{3} - \frac{a^2}{15D_{app}}j_m \tag{1}$$

Here, we define Q [mC $g_{(HC)}^{-1}$] as the reversible capacity of HC obtained at each applied current, C [mol dm^{-3}] as the concentration of the guest-ion in HC, a [cm] as the particle radius of HC, and j_m [mA $g_{(HC)}^{-1}$] as the current applied. The capacity decrease was proportional to the applied current, and D_{app} was estimated by using only the second term of eqn (1) and the linear parts of capacity decay (Fig. S6).[38] At slow rates involving both the slope capacity (adsorption/intercalation) and plateau capacity (pore-filling), D_{app} of the Na cell (5.7×10^{-11} cm^2 s^{-1}) was found to be faster than the Li cell (5.6×10^{-12} cm^2 s^{-1}). There is an additional capacity region with higher D_{app} (4.5×10^{-11} cm^2 s^{-1}) in the Li cell, which corresponds to the middle-potential region attributed to the lithium-insertion into the narrow interlayer space of the carbon planes.[2] At faster rates which mostly involve adsorption/

intercalation, D_{app} for Na and Li are quite similar at 5.8×10^{-10} and 5.1×10^{-10} cm^2 s^{-1}, respectively. The magnitude orders and trends of obtained values are consistent with previous reports of 10^{-10}–10^{-13} cm^2 s^{-1}.[40–42]

The polarization of the charge–discharge curves was further used to evaluate the charge-transfer resistance, R_{ct}, of the cells through Tafel plots. From the galvanostatic charge–discharge curves using 5 vol% HC-electrode, the cell voltages were extracted at capacities of 25 and 100 mAh g^{-1} during reduction and 100 and 200 mAh g^{-1} during oxidation (Fig. S7) to evaluate polarization in the slope and plateau regions, respectively. As shown in Fig. S8, these results are plotted as polarization (η) *versus* the applied current at the HC electrodes. η was determined by subtracting the voltage from (dis)charge curves measured at low currents. We note that the polarization of the counter electrode is negligible in the dilute electrode similar to single-particle measurements,[14,43] so the differences in η can be attributed to alkali-ion insertion/extraction at the HC-electrode. The obtained values of η for sodium insertion were smaller than those of lithium at high rates. Looking at the Tafel plots derived from de-sodiation/de-lithiation (oxidation) at 200 mAh g^{-1}, the Na cell showed larger polarization, which may be attributed to the increased resistivity at low SOC (Fig. S8a and right panel). R_{ct} can be estimated from the exchange current densities (j_0) as shown in eqn (2).[14]

$$R_{ct} = \frac{RT}{Fj_0} \tag{2}$$

where R is the gas constant, T is the temperature, and F is the Faraday constant. j_0 was obtained by extrapolation from the Tafel region in the η–log(j_m) plots at 25 mAh g^{-1} during insertion or at 100 mAh g^{-1} and 200 mAh g^{-1} during extraction. The estimated R_{ct} in the slope-capacity region at 25 mAh g^{-1} was 105–128 Ω mg$_{(HC)}$ in the Na cell and 103–114 Ω mg$_{(HC)}$ in the Li cell, respectively (Fig. S8a). Furthermore, the insertion plateau-capacity region at 100 mAh g^{-1} during extraction showed an R_{ct} of 70 Ω mg$_{(HC)}$ in the Na cell and 105 Ω mg$_{(HC)}$ in the Li cell, respectively (Fig. S8b). These results suggest that the exchange current density of Na^+ on sodiated HC can be comparable to or slightly higher than Li^+ on lithiated HC, relating to not only the electrochemical process at the electrode/electrolyte interfaces but also the SOC of HCs.[44,45] Tafel plots deviated from linearity at higher currents, implying the rate-limitation of mass transport in the HC particles.[14] Therefore, the rate-performance as shown in Fig. 4d and e can be majorly limited by the charge-transfer resistance.

As an additional comparison, we tested the rate capability of lithium intercalation using natural graphite flakes with the diluted electrode method as shown in Fig. S9. Using a 5 vol% graphite electrode, where rates are not limited by Li^+ supply, we could obtain 75% (at 755 mA g$_{(graphite)}{}^{-1}$) and 41% (at 1891 mA g$_{(graphite)}{}^{-1}$) of the capacity at low lithium-intercalation rates. The evaluated D_{app} based on rate-capability curves using eqn (S3) in the SI was 2.8×10^{-10} cm^2 s^{-1}. Overall, this indicates that the lithium diffusion coefficient into graphite is lower than the adsorption/intercalation of lithium and sodium at HC. On the other hand, our results also indicate that these rates are significantly faster than the pore-filling mechanism, which leaves a point of focus for future research to further enhance the power capabilities of HC for LIBs and SIBs. We have observed similar kinetic advantages for sodium in ether-based electrolytes (Fig. S10) using diethylene glycol dimethyl ether (G2), which is a well-known battery solvent that can form a robust and low resistive SEI on negative electrodes.[46,47] The electrolyte, consisting of 1 M $NaPF_6$ in G2, drastically improved the sodiation rate-capability alike to previous reports.[46] The 5 vol% HC electrodes maintained >90% capacity at 2500 mA g^{-1} (~10C) in the Na cell. In comparison, the Li cell containing 1.5 M lithium bis(fluorosulfonyl)amide dissolved in G2 also showed enhancement in lithiation but significantly less than the improvements observed with Na cells. Although detailed kinetic analysis of other electrolytes and the role of the SEI property is currently ongoing in our laboratory, these additional results further reinforce our conclusion that sodium insertion into this HC is intrinsically faster than lithium insertion.

Chronocoulometry and chronoamperometry

Next, we further investigated the kinetics of Na and Li insertion/extraction using potential step chronoamperometry (PSCA) at 5 vol% electrodes.[22,48] In this case, the potential control can be used to help separate the reactions corresponding to different storage sites by assuming the slope and plateau regions. Fig. S11a shows applied potential steps and the resulting chronoamperograms for the Na and Li cells. For the initial step from 1.0 V to 0.1 V regarding the slope region, the reduction currents reached *ca.* −7.5 A g^{-1} and quickly decayed to 0 A g^{-1}. As the potential was stepped lower to 0.002 V, which includes the plateau capacity, smaller currents of ~−1.0 A g^{-1} were observed (Fig. S11b). The Li cell showed higher current than the Na cell due to the larger capacity for adsorption/intercalation and electric double layer charging. Chronocoulograms showed good reversibility of capacity for slope and plateau regions, which are consistent with capacities collected using galvanostatic charge/discharge, $Q_{(GCD)}$ (see Fig. S12).

PSCA was also conducted at various temperatures as shown in Fig. 5a and b. The data were converted to chronocoulograms for the slope and plateau regions. To compare the reaction rate, the relaxation time (τ) for the formation of NaC_x or LiC_x, which is defined as the time when the capacity reached $Q_{(\tau)}$, is $1 - e^{-1}$ (63.2%) of the $Q_{(GCD)}$, which is collected in Table S3. The obtained τ are shown in Fig. 5c as a function of temperature. The resulting τ_{Na} and τ_{Li} showed an inverse relationship with temperature (40–10 °C) for the slope and plateau regions. Interestingly, the ratio between sodium- and lithium-insertion, τ_{Na}/τ_{Li}, was decreased, especially at lower temperatures (Fig. 5d). This implies that Na^+ insertion into hard carbon may be able to attain faster charging rates at lower temperatures. As is well known, relaxation time can provide a kinetic constant (k) and activation energy (E_a), following eqn (3) and (4), respectively:

$$\tau = \frac{1}{k} \tag{3}$$

$$E_a = \ln\left(\frac{1}{\tau}\right) \Big/ T \tag{4}$$

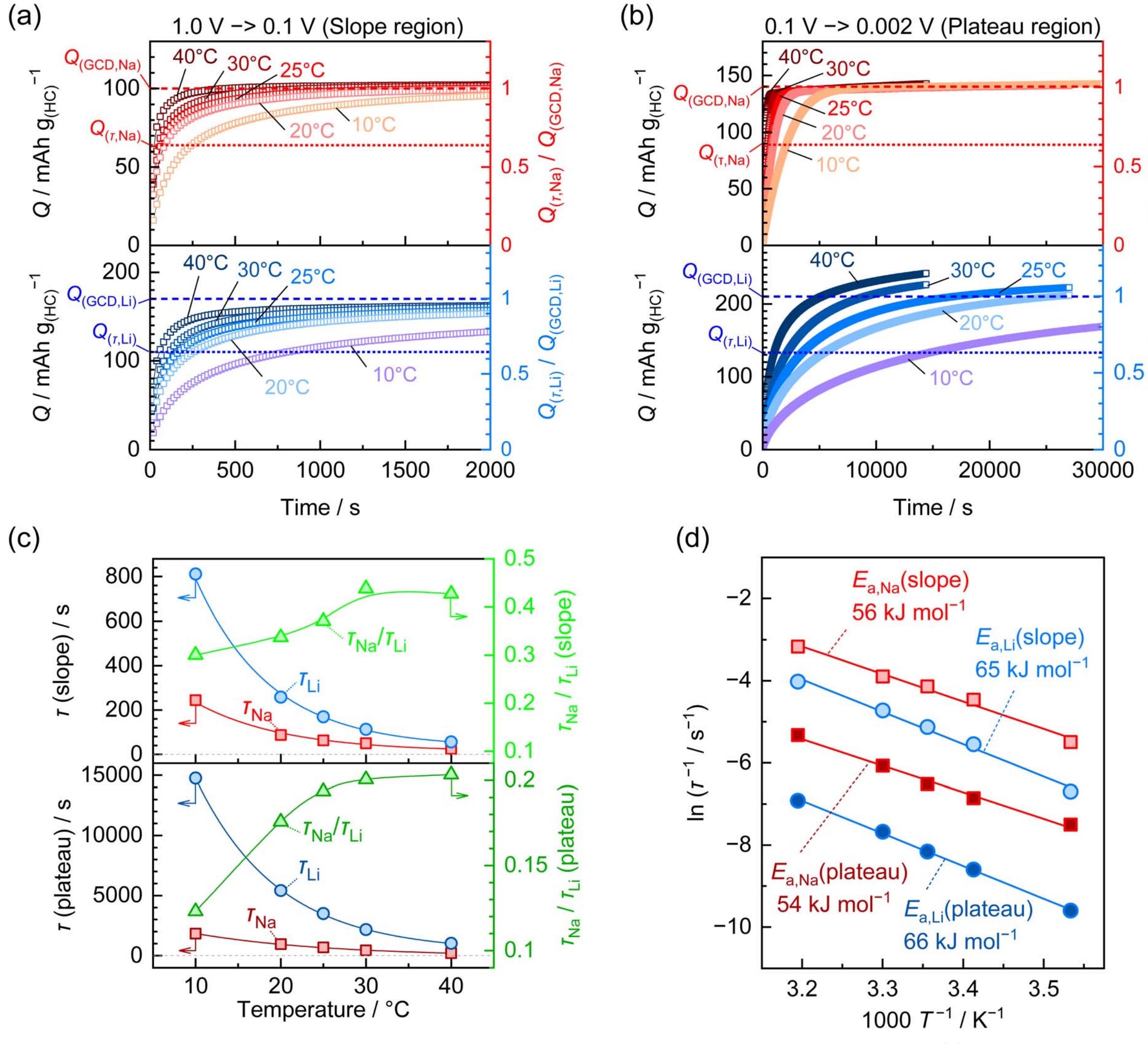

Fig. 5 PSCA for sodiation and lithiation of 5 vol% HC electrodes. Chronocoulograms corresponding to potential steps (a) from 1.0 V to 0.1 V and (b) from 0.1 V to 2 mV in Na and Li cells at various temperatures. (c) Relationships between the temperature and relaxation time of sodiation/lithiation obtained from chronocoulograms, and (d) the corresponding Arrhenius plot.

Fig. 5d shows the $\ln(\tau^{-1})-T^{-1}$ plot and estimated E_a. We found that the E_a for sodium insertion at 56 and 54 kJ mol^{-1} for the slope and plateau region were lower than that for lithium insertion at 65 and 66 kJ mol^{-1}.

Under PSCA, we can also evaluate D_{app} expressed by Fick's second law. Here, we estimate the D_{app} from linear parts of the $\ln(i)-t$ plots using a spherical model, as shown in eqn (5), assuming 5 vol% diluted electrodes behave like single-particle electrodes.[48–50] The equation is as follows:

$$\ln(i) = (-\pi^2 D_{app}/a^2)t + \ln(2nFAD_{app}\Delta C/a) \quad (5)$$

where a is the radius of the HC particles, t is the elapsed time after the potential step, n is the charge of the diffusing species, F is Faraday's constant, A is the surface area of the particle, and ΔC is the concentration change of guest-ion in particles induced by the potential step. Ideally, the applicable time range is often noted as greater than the diffusion-characteristic time, $a^2/\pi^2 D_{app}$, after obtaining the concentration gradient in the diffusion matrix. The most effective advantage of this model is that we can evaluate the D_{app} without the second term including the surface area and concentration, because the first term allows us to obtain D_{app} from the slope in $\ln(i)-t$ plots. Chronoamperograms obtained from PSCA at 25 °C are shown in Fig. 6 with their corresponding chronocoulograms. In both Na and Li cells, the current associated with the slope region showed a rapid decrease from $\ln(|i|) = -7$ to -10 within 500 s and a subsequent slow decay until 3000 s (Fig. 6a and b). The obtained $D_{app,\tau}$ values were 2.6×10^{-10} and 1.2×10^{-10} cm^2 s^{-1} at short times for 200 s and 300 s, respectively, which agreed with the results of the rate-capability testing (see Fig. S6). This rate decreased to 4.1×10^{-11} and 3.5×10^{-11} cm^2 s^{-1} ($D_{app,later}$) during the following slow decays after 760 s for sodium/lithium insertion, respectively.

When applying polarization in the plateau region, as shown in Fig. 6c and d, linear parts of $\ln(i)-t$ plots were observed implying solid-state diffusion from insertion and pore-filling.[3,6,7,10] Sodiation maintained high currents of $j_m > 100$ mA g^{-1} for 1200 s, followed by a current decay to 1 mA g^{-1} by 3000 s. The former fast current decay partially had smaller values of $a^2/\pi^2 D_{app}$ that implied a charge-transfer limiting process. We must keep in mind some ambiguity in isolating these different processes, but the obtained $D_{app,\tau}$ and $D_{app,later}$ were 2.5×10^{-11} and 5.0×10^{-11} cm^2 s^{-1}, respectively. This current behavior is similar to the lithium insertion of $Li_{4/3}Ti_{5/3}O_4$ reported by Takami *et al.*;[15] therefore, we also used a core–shell model for gaining kinetic insight of the plateau region. $D_{app,\tau}$ and $D_{app,later}$ for lithiation were 5.2×10^{-12} and 3.0×10^{-12} cm^2 s^{-1}, respectively, in good agreement with the rate-capability tests.

The temperature dependence of chronoamperograms and D_{app} was further investigated, as shown in Fig. S13 and S14, respectively. The $\log(D_{app})$–T^{-1} plots are shown in Fig. 6e and f. Both Na and Li cells showed similar results to room temperature measurements with almost the same shape for the chronoamperograms between 10 and 40 °C. D_{app} for the slope region

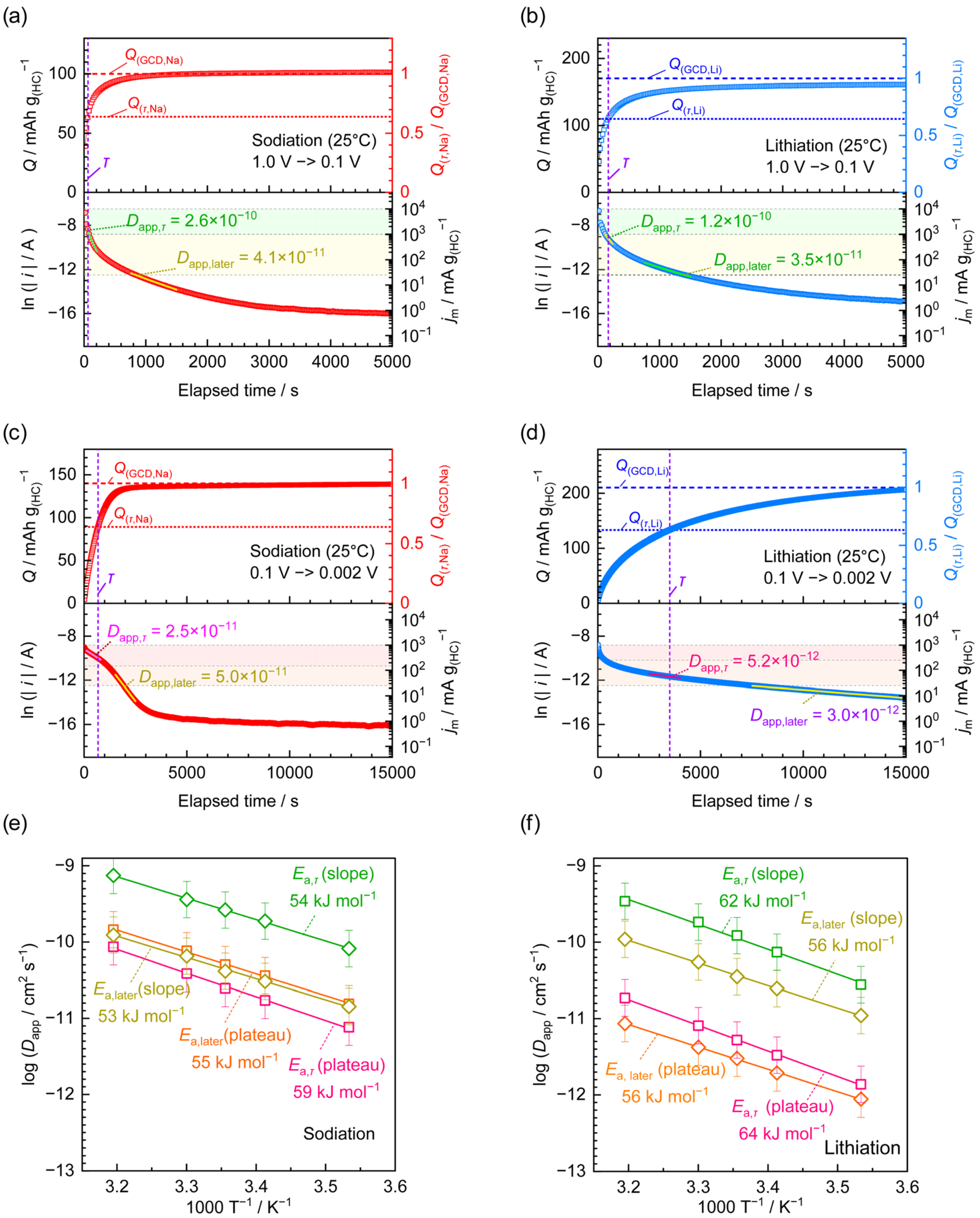

Fig. 6 Chronocoulograms and corresponding chronoamperograms of 5 vol% HC electrodes for the slope regions of (a) sodiation and (b) lithiation and plateau regions of (c) sodiation and (d) lithiation. The values of D_{app} were estimated by applying eqn (4), as described in the Experimental section. Activation energies $E_{a,\tau}$ and $E_{a,later}$ were estimated from D_{app} *vs.* T^{-1} plots of $D_{app,\tau}$ and $D_{app,later}$ during (e) sodiation and (f) lithiation, respectively. The error bars of D_{app} values are estimated from standard error of the HC particle size.

varied between ~10^{-10} and 10^{-11} cm^2 s^{-1} for both sodium and lithium insertion. These results agree well with self-diffusion coefficients obtained from positive-muon spin relaxation at ~10^{-10}–10^{-11} cm^2 s^{-1} for NaC_x (HC), LiC_6 (graphite) and LiC_{12} (graphite) in our previous reports.[51,52] On the other hand, the plateau region delivered a slower diffusion coefficient in ~10^{-10}–10^{-12} cm^2 s^{-1}, which is consistent with charge/discharge rate testing where the plateau region becomes inaccessible at high rates due to complex kinetic factors, *i.e.*, nucleation of pseudo-metallic clusters. Fig. 6e and f show the corresponding E_a calculated using eqn (6)[53]

$$D_{app} = A\ \exp\left(-\frac{E_a}{k_B T}\right) \tag{6}$$

where A is the pre-exponential factor, k_B is the Boltzmann constant, and T is the temperature. We found E_a for sodium insertion at 53–54 and 55–59 kJ mol^{-1} for the slope and plateau regions, respectively, and for lithium insertion at 56–62 and 56–64 kJ mol^{-1}, respectively, consistent with the E_a obtained from the τ of the chronocoulogram (Fig. 5d).

Electrochemical impedance spectroscopy

As a final analysis of these two systems, we focused on EIS, as shown in the Nyquist plots for the Na and Li cells (Fig. 7) using 95, 40 and 5 vol% HC-electrode concentrations. The EIS measurements were performed at OCVs of 0.5 V, 0.06 V and 0.015 V during the 5th galvanostatic charge/discharge cycle. Aside from the half-cell, we also evaluated the impedance of symmetric cells of Na or Li metal disks, as shown in Fig. S15. According to the frequency response in the half-cell and symmetric cell, the semicircles at higher and lower frequencies are mostly attributed to the counter and working electrodes, respectively.[54]

Moving from the OCV to 0.5 V, all cells showed a decreased impedance at low frequencies with electrochemical reduction of HC, as previously reported.[54,55] Interestingly, cells using electrodes with a higher HC concentration, *i.e.*, 95 and 40 vol% in Fig. 7a and b, showed an increase in resistance at 0.06 V and 0.015 V. Furthermore, expansion of the semicircle was observed between 2000 and 1 Hz in the Na cell and an additional semicircle developed between 1 and 0.01 Hz in the Li cell, regardless of whether there were dilutants. Even in 3-electrode cells using 40 vol% HC-electrodes (Fig. S16a and b), the increase in impedance was pronounced after reaching potentials corresponding to the plateau region in both Na and Li cells, lower than 0.06 V *vs.* Na^+/Na and 0.015 V *vs.* Li^+/Li, respectively. Simultaneously, as shown in magnified Nyquist plots (Fig. S16c and d) and Bode plots (Fig. S17), there were apparent expansions of the higher frequency semicircle at >100 Hz, which we can attribute to guest-ion transportation in porous structures,[56] contact resistance between particles,[57–59] and inhomogeneities of SOC.[45,60–62] Interestingly, during the extraction process, as shown in Fig. S16e–h, the impedance decreased until 0.08 V and then increased again at 0.6 V, especially in the Na cell. We speculate that the increasing impedance at a higher HC concentration may be caused by an inhomogeneous SOC distribution of the HC particles throughout the composite electrode, which occurs due to the guest-ion depletion (Fig. 4a) during the insertion process. This drastic guest-ion consumption could be a factor that results in lower rate capabilities of the Na cell; therefore, it should be considered when designing the high-power HC electrode for optimizing the fast transport of solvated Na^+ in the electrolyte.[33,63]

On the other hand, using 5 vol% HC-electrode (Fig. 7c) that can suppress the concentration overvoltage in the electrolyte led to smaller impedance during electrochemical reduction from 0.5 V

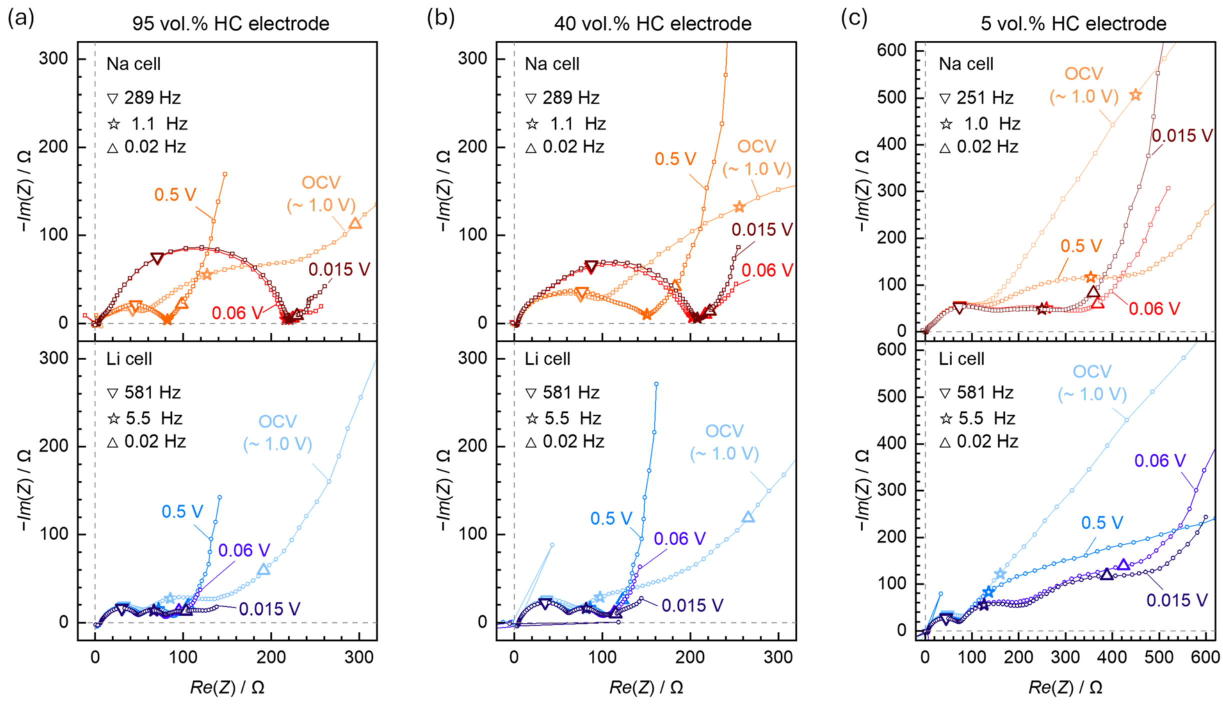

Fig. 7 Nyquist plots of electrochemical impedance obtained in the 5th cycle of Na and Li cells with (a) 95, (b) 40, and (c) 5 vol% HC electrodes.

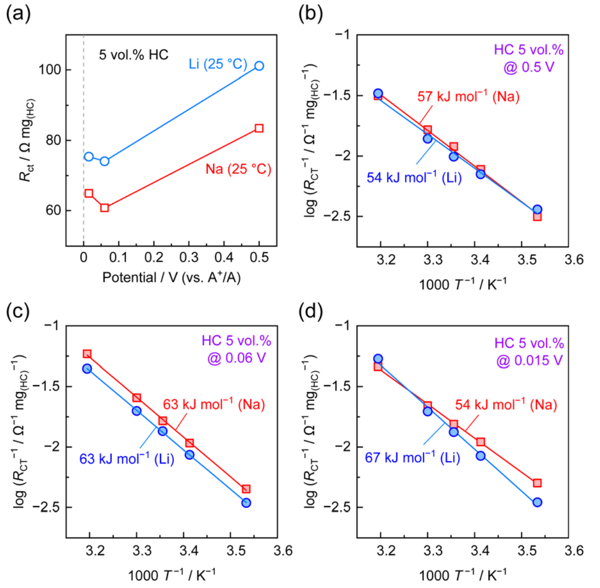

Fig. 8 (a) R_{ct} values of 5 vol% HC electrodes evaluated by fitting electrochemical impedance spectra obtained after high-current tests. Log(R_{ct}^{-1})–T^{-1} plots collected at (b) 0.5 V, (c) 0.06 V, and (d) 0.015 V.

to 0.06 V. Simultaneously, the total impedance becomes larger up to 600 Ω because of the low loading of HC. The Na cell showed an unclear semicircle attributed to HC at frequencies lower than 25 Hz and was difficult to deconvolute to two parallel components with good reproducibility. Fig. S18 and S19 show the Nyquist plots of cycled electrodes (after high-current testing). We used the equivalent circuit shown in Fig. S20a for analysis regarding the wide semicircle located around 1 Hz. A slightly different equivalent circuit, shown in Fig. S20b, was applied to the Li cell to accommodate the larger semicircles located around 5.5 Hz and 20 mHz, attributed to HC and side reactions of other components such as SWCNTs, respectively. Also, to accommodate the absence of capacitive behavior at lower frequencies, Fig. 8 and Table S4 show evaluated R_{ct} values which were normalized based on the HC mass. The resistance values obtained at 25 °C and 0.5 V with 83 Ω $mg_{(HC)}$ in Na cells and 101 Ω $mg_{(HC)}$ in Li cells were consistent with the R_{ct} estimated from Tafel plots (see Fig. S8). When the electrodes were electrochemically reduced from 0.5 V to 0.06 V, both cells showed a decrease in their R_{ct}, and those values remained nearly constant after further reduction to 0.015 V as reported previously.[40] Through log(R_{ct}^{-1})–T^{-1} plots shown in Fig. 8b and c, we found that sodiated-HC at a higher SOC (0.06 V and 0.015 V) has a smaller R_{ct} compared to lithiated-HC in agreement with our PSCA results (Fig. 5c). E_a values were extracted from log(R_{ct}^{-1})–T^{-1} plots using eqn (7):[40]

$$R_{ct}^{-1} = A\exp\left(-\frac{E_a}{RT}\right) \tag{7}$$

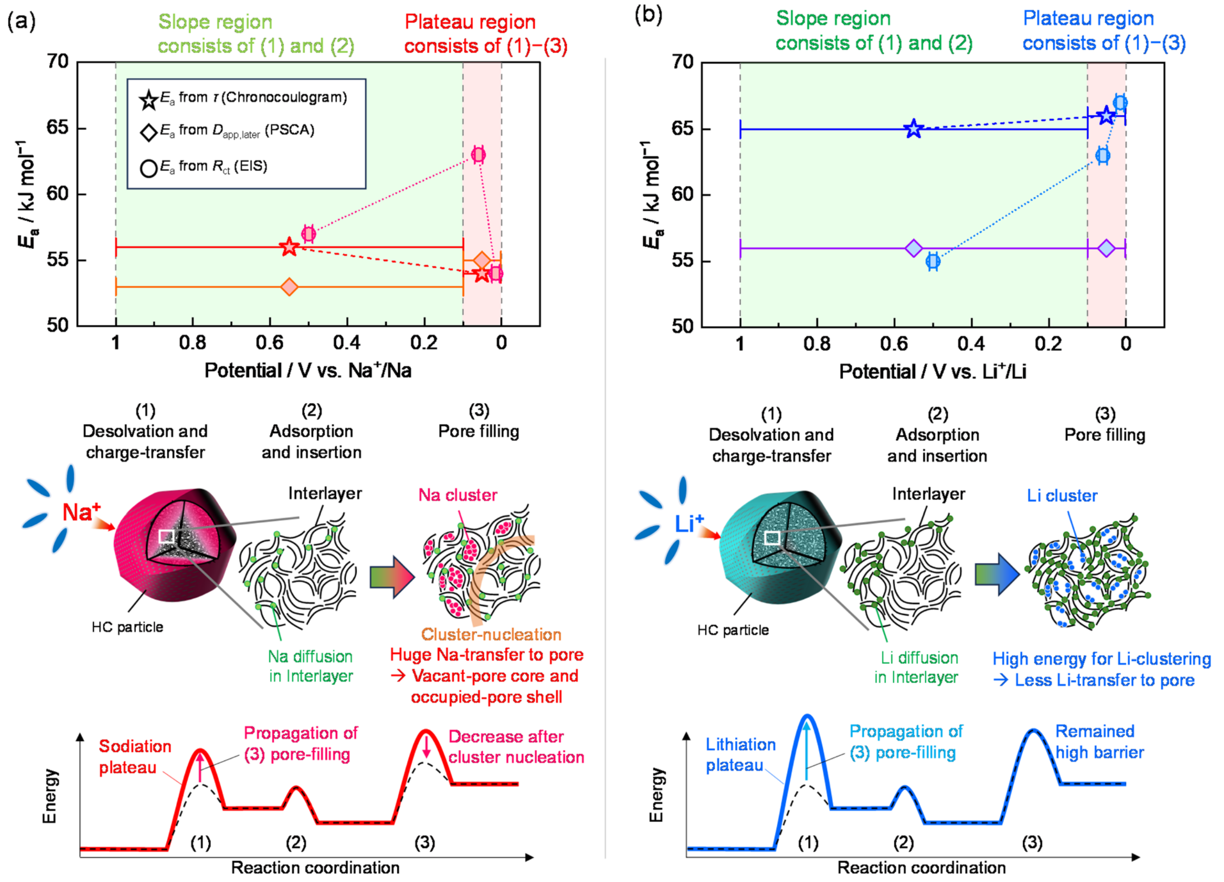

Fig. 9 The summarized results of E_a for (a) sodiation and (b) lithiation of HC from our various measurements; E_a during the insertion process obtained from the τ of chronocoulogram, $D_{app,later}$ estimated from PSCA, and R_{ct} evaluated by EIS.

Here, A is the pre-exponential constant and R is the universal gas constant. Electrochemical reduction from 0.5 V and 0.06 V increased the E_a in both Na (57 kJ mol^{-1}) and Li cells (54 kJ mol^{-1}) to 63 kJ mol^{-1}. However, upon further reduction to 0.015 V the E_a increased for lithiation while decreasing for sodiation, as summarized in Fig. 9. We can regard that values of E_a during the insertion process obtained from the τ of chronocoulogram, $D_{app,later}$ estimated from PSCA, and R_{ct} evaluated by EIS represent the entire reaction in the slope/plateau region, the solid-state diffusion, and the charge-transfer, respectively. Evaluating the E_a of Na insertion using R_{ct} provided similar results to that obtained from τ in eqn (4) for the slope region from 1.0 V to 0.1 V. On the other hand, E_a increased in the middle of the plateau at 0.06 V. Finally, these E_a values converged to the same order in the E_a of $D_{app,later}$ at 0.015 V at the end of the plateau (Fig. 9a). This result implies that the plateau region accompanying pseudo-metallic cluster formation becomes the rate-determining step for full sodiation of HC. Furthermore, it can suppress the kinetics of other elemental reactions, *i.e.*, desolvation and diffusion of sodium ions/atoms in a pseudographitic layer[40] during propagation of the cluster into inner pores like the core–shell model,[15] as illustrated in the reaction coordinates. On the other hand, a greater E_a attributed to τ and R_{ct} for Li insertion was observed even at the lowest potential, implying that the higher energy for Li clustering can limit the Li-insertion rate in the plateau region, and there might be homogeneous filling into the inner pores not following the core–shell model.

In total, our various results indicate that sodium insertion into this HC is faster than lithium insertion. Here, the origin of this advantage of sodiation is speculated as follows: (i) weak interaction between sodium atoms and defects in the graphene sheet, (ii) less sodium atom occupancy in the interlayer space, and (iii) less nucleation energy of the pseudo-metal clustering within the nanopores. For point (i), DFT calculations indicate that lithium has stronger interactions with carbon than sodium.[24,64–66] The HC used in this study also contains sulfur at elemental compositions of ~1 wt%, as shown in Fig. S2c, which may form sulfur-containing defects in the graphitic interlayers. Like carbon, these sulfur defects may show weaker interactions with sodium that enable easier sodium ion migration in the vicinity of the defects compared with lithium.[67] For point (ii), according to reports revealing the storage site, less sodium is stored in the interlayer space of HC compared with Li^+.[2,66] The reported selectiveness of this storage site in HCs may enhance sodium diffusion and prevent trapping. Finally, for point (iii), Li *et al.*,[24] Morita and Gotoh *et al.*[7,64] have reported that pseudo-metallic Na clusters are more energetically favorable in HCs with similar micropore size as our HC. In addition, Aniskevich *et al.* found that sodium diffusion includes transport from the interlayer to the pore that can limit the sodiation rate.[54] Our estimated activation energies obtained from temperature testing are consistent with previous results.

Conclusions

In this study, we have used the diluted electrode method to deeply investigate the kinetics of sodiation and lithiation at HC. Based on charge/discharge testing, CV and PSCA under temperature control, the solid-state diffusion in HC is found to be faster than liquid-state transportation within the electrolyte found inside the composite electrode porous network. This leads to serious rate-limitations with inhomogeneous SOC across the composite electrode bulk. In diluted HC-electrodes, Na cells showed remarkably higher rate-performance than Li, where we could obtain 80% and 40% of the full capacity at rates of 1000 and 2500 mA $g_{(HC)}{}^{-1}$, respectively, with proper accessibility to the plateau region. For the Li case, we found less impact by using the dilute electrode method with rapid fading to ~60% at low charging rates of 200 mA g^{-1}. However, the undiluted electrodes showed good rate capability that remained >40% up to 1000 mA g^{-1} for lithiation, which improved over sodiation at the undiluted HC-electrode, showing a capacity of only 40% up to ~100 mA $g_{(HC)}{}^{-1}$. This discretion likely depends on the contribution of complex resistances associated with the composite-electrode structure as rate-limiting. Overall, the rate capability of sodium insertion was determined to be faster and show less impedance compared with lithium insertion at the same HC, as well as comparable to the lithium intercalation into diluted graphite electrodes. The estimated D_{app} and E_a for sodiation and lithiation showed differences in pseudo-metallic cluster nucleation during pore-filling, but similar Na^+- and Li^+-diffusion rates during adsorption and insertion into the interlayer. Our results suggest that interesting capabilities for fast sodiation of HC can be investigated by the dilute electrode method and a core–shell model, which may be similar to the high-capacity HCs developed in our laboratory. Further studies related to the HC structure,[11] electrolyte, electrolyte additives, binder, and other alkali-metal ions *i.e.*, K^+,[68] Rb^+,[69] and Cs^+,[70] furthermore, alloys,[71] layered oxides, polyanion compounds, and Prussian blue analogues,[34,63,72] are currently ongoing.

Author contributions

Y. F.: conceptualization, investigation, writing – original draft; Z. T. G. and R. T.: investigation, writing – review & editing; S. K.: supervision, investigation, writing – review & editing.

Conflicts of interest

The authors declare no competing interests.

Data availability

The datasets in the current study are available from the corresponding author on reasonable request.

Supplementary information (SI): characterization of hard carbon using XRD, SAXS, elemental analysis, and particle size distribution analysis; additional characterization of diluted electrode, electronic conductivities, SEM-EDX mapping; details and table of gravimetric capacity correction for SWCNTs; details of evaluation for D_{app} and polarization during rate testing; electrochemical tests in glyme electrolytes; supporting data of PSCA and chronoamperograms collected at various temperature; electrochemical impedances of alkali metal disks, 40 vol% HC electrode in 3-electrode cells; Nyquist plots of 5 vol% HC electrode collected at various temperature, equivalent circuit for EIS analysis, and evaluated R_{ct}. See DOI: https://doi.org/10.1039/d5sc07762a.

Acknowledgements

The authors gratefully appreciate Ms Rena Takaishi and Mr Takashi Matsuyama from NIPPON A&L INC. for their fruitful discussion and Assoc. Prof. Kingo Ariyoshi from Osaka Metropolitan University for his instruction and discussion about the diluted electrode method. Y. F. thanks Ms Ayame Sasaki and Mr Tadanori Kawamata for their experimental support and Dr Daisuke Igarashi and Dr Tomooki Hosaka for their assistance in manuscript preparation. This study was partially funded by the Ministry of Education, Culture, Sports, Science and Technology (MEXT) Program: Data Creation and Utilization Type Materials Research (JPMXP1122712807), the JST through CREST (JPMJCR21O6), ASPIRE (JPMJAP2313), GteX (JPMJGX23S4), JSPS KAKENHI (JP25H00905, JP24H00042, and JP23H01693) and JSPS-Grant-in-Aid for JSPS Fellows (JP24KJ2024).

References

1 Z. T. Gossage, D. Igarashi, Y. Fujii, M. Kawaguchi, R. Tatara, K. Nakamoto and S. Komaba, *Chem. Sci.*, 2024, **15**, 18272–18294.

2 K. Kubota, S. Shimadzu, N. Yabuuchi, S. Tominaka, S. Shiraishi, M. Abreu-Sepulveda, A. Manivannan, K. Gotoh, M. Fukunishi, M. Dahbi and S. Komaba, *Chem. Mater.*, 2020, **32**, 2961–2977.

3 J. M. Stratford, A. K. Kleppe, D. S. Keeble, P. A. Chater, S. S. Meysami, C. J. Wright, J. Barker, M.-M. Titirici, P. K. Allan and C. P. Grey, *J. Am. Chem. Soc.*, 2021, **143**, 14274–14286.

4 H. Hijazi, Z. Ye, E. Zsoldos, M. Obialor, W. Black, S. Azam, J. R. Dahn and M. Metzger, *J. Electrochem. Soc.*, 2024, **171**, 050521.

5 D. Igarashi, Y. Tanaka, K. Kubota, R. Tatara, H. Maejima, T. Hosaka and S. Komaba, *Adv. Energy Mater.*, 2023, **13**, 2302647.

6 Y. Morikawa, S. Nishimura, R. Hashimoto, M. Ohnuma and A. Yamada, *Adv. Energy Mater.*, 2020, **10**, 1903176.

7 K. Gotoh, M. Maeda, A. Nagai, A. Goto, M. Tansho, K. Hashi, T. Shimizu and H. Ishida, *J. Power Sources*, 2006, **162**, 1322–1328.

8 C.-W. Tai, W.-Y. Jao, L.-C. Tseng, P.-C. Wang, A.-P. Tu and C.-C. Hu, *J. Mater. Chem. A*, 2023, **11**, 19669–19684.

9 N. Takami, A. Satoh, M. Hara and T. Ohsaki, *J. Electrochem. Soc.*, 1995, **142**, 371–379.

10 K. Gotoh, T. Yamakami, I. Nishimura, H. Kometani, H. Ando, K. Hashi, T. Shimizu and H. Ishida, *J. Mater. Chem. A*, 2020, **8**, 14472–14481.

11 Y. Fujii, H. Yoshimo, R. Tatara, Z. T. Gossage, A. Koizumi and S. Komaba, *ACS Appl. Energy Mater.*, 2025, **8**, 6577–6585.

12 Y. Orikasa, Y. Gogyo, H. Yamashige, M. Katayama, K. Chen, T. Mori, K. Yamamoto, T. Masese, Y. Inada, T. Ohta, Z. Siroma, S. Kato, H. Kinoshita, H. Arai, Z. Ogumi and Y. Uchimoto, *Sci. Rep.*, 2016, **6**, 26382.

13 K. Kitada, H. Murayama, K. Fukuda, H. Arai, Y. Uchimoto, Z. Ogumi and E. Matsubara, *J. Power Sources*, 2016, **301**, 11–17.

14 K. Dokko, N. Nakata, Y. Suzuki and K. Kanamura, *J. Phys. Chem. C*, 2010, **114**, 8646–8650.

15 N. Takami, K. Hoshina and H. Inagaki, *J. Electrochem. Soc.*, 2011, **158**, A725–A730.

16 J. Suzuki, N. Kubota, Y. Omura, K. Sugata, K. Kisa, H. Sofuji and M. Hattori, *Electrochemistry*, 2018, **86**, 116–121.

17 Y. Fujii, K. Sugata, Y. Omura, N. Kubota, K. Kisa, H. Sofuji and J. Suzuki, *Electrochemistry*, 2023, **91**, 077008.

18 K. Ariyoshi, S. Mizutani, T. Makino and Y. Yamada, *J. Electrochem. Soc.*, 2018, **165**, A3965–A3970.

19 K. Ariyoshi, J. Sugawa and S. Masuda, *J. Electrochem. Soc.*, 2020, **167**, 140517.

20 K. Ariyoshi, J. Sugawa and S. Masuda, *J. Power Sources*, 2021, **509**, 230349.

21 K. Ariyoshi and J. Sugawa, *Electrochim. Acta*, 2023, **455**, 142425.

22 K. Ariyoshi and S. Hiroshima, *Electrochim. Acta*, 2024, **487**, 144192.

23 Y. Fujii, R. Tatara, D. Igarashi, T. Hosaka, R. Takaishi, E. Shiiyama, T. Matsuyama and S. Komaba, *Electrochemistry*, 2023, **91**, 077002.

24 Y. Li, A. Vasileiadis, Q. Zhou, Y. Lu, Q. Meng, Y. Li, P. Ombrini, J. Zhao, Z. Chen, Y. Niu, X. Qi, F. Xie, R. van der Jagt, S. Ganapathy, M.-M. Titirici, H. Li, L. Chen, M. Wagemaker and Y.-S. Hu, *Nat. Energy*, 2024, **9**, 134–142.

25 Kureha Battery Materials Japan Co., Ltd, *High-performance Anode Material CARBOTRON® P*, https://www.kureha.co.jp/development/story/pdf/catalog_hc_eg_20120924.pdf, accessed 2023/04/30.

26 FUJIFILM Wako Pure Chemical Corporation, *SAFETY DATA SHEET Aluminium Oxide*, https://labchem-wako.fujifilm.com/sds/W01W0101-0196JGHEEN.pdf, accessed 2025/09/29.

27 International Chemical Safety Card, *Polyacrylic Acid, Sodium Salt*, https://www.ilo.org/dyn/icsc/showcard.display?p_card_id=1429&p_version=2&p_lang=en, accessed 2023/04/30.

28 H. Kondo, H. Sawada, C. Okuda and T. Sasaki, *J. Electrochem. Soc.*, 2019, **166**, A1285–A1290.

29 R. Tian, N. Alcala, S. J. K. O'Neill, D. V. Horvath, J. Coelho, A. J. Griffin, Y. Zhang, V. Nicolosi, C. O'Dwyer and J. N. Coleman, *ACS Appl. Energy Mater.*, 2020, **3**, 2966–2974.

30 T. Yamamoto, T. Yamaguchi, T. Nohira, R. Hagiwara, A. Fukunaga, S. Sakai and K. Nitta, *Electrochemistry*, 2017, **85**, 391–396.

31 S. Komaba, W. Murata, T. Ishikawa, N. Yabuuchi, T. Ozeki, T. Nakayama, A. Ogata, K. Gotoh and K. Fujiwara, *Adv. Funct. Mater.*, 2011, **21**, 3859–3867.

32 H. Hijazi, Z. Ye, L. Zhang, J. Deshmukh, M. B. Johnson, J. R. Dahn and M. Metzger, *J. Electrochem. Soc.*, 2023, **170**, 070512.

33 J. Landesfeind, T. Hosaka, M. Graf, K. Kubota, S. Komaba and H. A. Gasteiger, *J. Electrochem. Soc.*, 2021, **168**, 040538.

34 E. J. Kim, P. R. Kumar, Z. T. Gossage, K. Kubota, T. Hosaka, R. Tatara and S. Komaba, *Chem. Sci.*, 2022, **13**, 6121–6158.

35 S. Tsujimoto, Y. Kondo, Y. Yokoyama, Y. Miyahara, K. Miyazaki and T. Abe, *J. Electrochem. Soc.*, 2021, **168**, 070508.

36 R. Mogensen, D. Brandell and R. Younesi, *ACS Energy Lett.*, 2016, **1**, 1173–1178.

37 T. Takamura, *Electrochemistry*, 2012, **80**, 3–14.

38 K. Ariyoshi and J. Sugawa, *Electrochemistry*, 2021, **89**, 157–161.

39 M. Okubo, Y. Tanaka, H. Zhou, T. Kudo and I. Honma, *J. Phys. Chem. B*, 2009, **113**, 2840–2847.

40 Y. Aniskevich, J. H. Yu, J. Kim, S. Komaba and S. Myung, *Adv. Energy Mater.*, 2024, 2304300.

41 Z. Guo, Z. Xu, F. Xie, J. Jiang, K. Zheng, S. Alabidun, M. Crespo-Ribadeneyra, Y. Hu, H. Au and M. Titirici, *Adv. Mater.*, 2023, **35**, 2304091.

42 D. Ledwoch, L. Komsiyska, E.-M. Hammer, K. Smith, P. R. Shearing, D. J. L. Brett and E. Kendrick, *Electrochim. Acta*, 2022, **401**, 139481.

43 K. Ando, M. Tsuta and K. Kanamura, *J. Electroanal. Chem.*, 2023, **948**, 117802.

44 S. R. Narayanan, D. H. Shen, S. Surampudi, A. I. Attia and G. Halpert, *J. Electrochem. Soc.*, 1993, **140**, 1854–1861.

45 N. Takami, A. Satoh, M. Hara and T. Ohsaki, *J. Electrochem. Soc.*, 1995, **142**, 371–379.

46 R. Dong, L. Zheng, Y. Bai, Q. Ni, Y. Li, F. Wu, H. Ren and C. Wu, *Adv. Mater.*, 2021, **33**, 2008810.

47 X. Yi, X. Li, J. Zhong, S. Wang, Z. Wang, H. Guo, J. Wang and G. Yan, *Adv. Funct. Mater.*, 2022, 2209523.

48 M. Nishizawa, *Electrochem. Solid-State Lett.*, 1999, **1**, 10.

49 M. Nishizawa, H. Koshika, R. Hashitani, T. Itoh, T. Abe and I. Uchida, *J. Phys. Chem. B*, 1999, **103**, 4933–4936.

50 K. Dokko, M. Mohamedi, M. Umeda and I. Uchida, *J. Electrochem. Soc.*, 2003, **150**, A425–A429.

51 K. Ohishi, D. Igarashi, R. Tatara, S. Nishimura, A. Koda, S. Komaba and J. Sugiyama, *ACS Phys. Chem. Au*, 2022, **2**, 98–107.

52 I. Umegaki, S. Kawauchi, H. Sawada, H. Nozaki, Y. Higuchi, K. Miwa, Y. Kondo, M. Månsson, M. Telling, F. C. Coomer, S. P. Cottrell, T. Sasaki, T. Kobayashi and J. Sugiyama, *Phys. Chem. Chem. Phys.*, 2017, **19**, 19058–19066.

53 S. Yang, B. Yan, J. Wu, L. Lu and K. Zeng, *ACS Appl. Mater. Interfaces*, 2017, **9**, 13999–14005.

54 Y. Aniskevich, J. H. Yu, J. Kim, S. Komaba and S. Myung, *Adv. Energy Mater.*, 2024, 2304300.

55 G. Hasegawa, K. Kanamori, N. Kannari, J. Ozaki, K. Nakanishi and T. Abe, *J. Power Sources*, 2016, **318**, 41–48.

56 F. Linsenmann, D. Pritzl and H. A. Gasteiger, *J. Electrochem. Soc.*, 2021, **168**, 010506.

57 K. Ariyoshi, S. Mizutani and Y. Yamada, *J. Power Sources*, 2019, **435**, 226810.

58 K. Ariyoshi, M. Tanimoto and Y. Yamada, *Electrochim. Acta*, 2020, **364**, 137292.

59 H. Nara, K. Morita, D. Mukoyama, T. Yokoshima, T. Momma and T. Osaka, *Electrochim. Acta*, 2017, **241**, 323–330.

60 E. Barsoukov, J. H. Kim, J. H. Kim, C. O. Yoon and H. Lee, *Solid State Ionics*, 1999, **116**, 249–261.

61 H. Nara, D. Mukoyama, T. Yokoshima, T. Momma and T. Osaka, *J. Electrochem. Soc.*, 2016, **163**, A434–A441.

62 H. Kim, S. K. Oh, J. Lee, S. W. Doo, Y. Kim and K. T. Lee, *Electrochim. Acta*, 2021, **370**, 137743.

63 T. Hosaka, K. Kubota, A. S. Hameed and S. Komaba, *Chem. Rev.*, 2020, **120**, 6358–6466.

64 R. Morita, K. Gotoh, M. Fukunishi, K. Kubota, S. Komaba, N. Nishimura, T. Yumura, K. Deguchi, S. Ohki, T. Shimizu and H. Ishida, *J. Mater. Chem. A*, 2016, **4**, 13183–13193.

65 Q. Li, J. Zhang, L. Zhong, F. Geng, Y. Tao, C. Geng, S. Li, B. Hu and Q. Yang, *Adv. Energy Mater.*, 2022, **12**, 2201734.

66 H. Kim, J. C. Hyun, D.-H. Kim, J. H. Kwak, J. B. Lee, J. H. Moon, J. Choi, H.-D. Lim, S. J. Yang, H. M. Jin, D. J. Ahn, K. Kang, H.-J. Jin, H.-K. Lim and Y. S. Yun, *Adv. Mater.*, 2023, **35**, 2209128.

67 E. Olsson, G. Chai, M. Dove and Q. Cai, *Nanoscale*, 2019, **11**, 5274–5284.

68 S. Komaba, T. Hasegawa, M. Dahbi and K. Kubota, *Electrochem. Commun.*, 2015, **60**, 172–175.

69 D. Igarashi, R. Tatara, R. Fujimoto, T. Hosaka and S. Komaba, *Chem. Sci.*, 2023, **14**, 11056–11066.

70 A. Yadav, H. Kobayashi, T. Yamamoto and T. Nohira, *Electrochemistry*, 2024, **92**, 043008.

71 S. Yamazaki, R. Tatara, H. Mizuta, K. Kawano, S. Yasuno and S. Komaba, *Mater. Adv.*, 2023, **4**, 1637–1647.

72 N. Yabuuchi, K. Kubota, M. Dahbi and S. Komaba, *Chem. Rev.*, 2014, **114**, 11636–11682.